RESEARCH PAPER

Acta Neurobiol Exp 2026, 86: 139–145
DOI: 10.55782/2hr5ac70

Lightweight CNN recognition of HeLa cell PCNA-based S-phase subphases and RFC-dependent dynamics

Maciej Krupa* and Jędrzej Szymański

Laboratory of Imaging of Tissue Structure and Function, Nencki Institute of Experimental Biology, Polish Academy of Sciences, Warsaw, Poland
** Email: maciek.w.krupa@gmail.com*

Proliferating cell nuclear antigen (PCNA) forms subnuclear replication patterns that report S-phase progression with a single marker and provide an imaging readout of the replication factor C (RFC)-PCNA axis. We benchmarked lightweight convolutional neural networks for classifying fixed HeLa cell PCNA images as G1, early S, mid S, or late S, and then applied the best-performing model to live-cell RFC control and RFC-del datasets. MobileNetV2 provided the best balance of accuracy and inference cost in the fixed-cell benchmark. In live-cell traces, RFC-del cells showed prolonged late S-like PCNA pattern duration, whereas mid S-like duration and peak-distance metrics did not show clear group separation. These findings support lightweight PCNA-pattern classification as a practical tool for quantitative replication-pattern phenotyping and indicate a possible future application to neurobiological imaging, such as automated quantification of proliferating cells in neurogenesis studies.

Key words: PCNA; S-phase; HeLa cells; lightweight convolutional neural networks; replication factor C; live-cell imaging; neurogenesis

INTRODUCTION

PCNA is a sliding clamp that accumulates at replication sites and produces characteristic nuclear patterns during early S, mid S, and late S. Single-marker PCNA imaging is useful when additional fluorescence channels must remain available for proteins of interest, but the resulting patterns still require reliable classification (Kelman, 1997; Zerjatke et al., 2017).

Earlier cell-cycle reporters used several fluorescent channels to separate phases. In contrast, endogenous PCNA tracking can classify G1, G2, M, and G0 states from expression and localization dynamics while preserving spectral space for other markers (Zerjatke et al., 2017). PCNA also participates in DNA repair, chromatin remodeling, and replication-fork biology, so its interpretation benefits from mechanistic context (Essers et al., 2005; Moldovan et al., 2007; Li et al., 2018).

RFC is the canonical clamp loader that opens and loads the PCNA trimer onto DNA. RFC-del denotes an RFC1/p140 DNA-binding-domain deletion mutant lacking residues 367-493, based on the RFC140 domain mapping described by Hashiguchi et al. (2007). For this reason, changes in PCNA foci during live-cell imaging are relevant to the RFC-PCNA axis and can be used to test whether RFC perturbation is associated with altered timing of PCNA-defined replication patterns (Hashiguchi et al., 2007; Yao & O'Donnell, 2012).

PCNA is widely used as a marker of DNA replication and cell proliferation. Consequently, automated recognition of PCNA patterns may be useful not only in cancer cell biology but also in biological systems in which proliferating cell populations must be quantified from microscopy images. Such applications include studies of neural stem and progenitor cells during embryonic and adult neurogenesis, where PCNA is routinely used as an indicator of cell-cycle progression (Zhang & Jiao,

Received 18 June 2026, accepted 16 July 2026

2015). Although the present work focuses on HeLa cells, the computational framework developed here may provide a basis for future adaptation to neurobiological imaging datasets.

Schönenberger et al. (2015) previously classified PCNA-immunolabeled cells using hand-engineered image descriptors and classical machine learning. Haralick texture features were among the descriptors used to quantify spatial relationships between pixel intensities before classification (Haralick et al., 1973).

Deep learning removes much of the manual feature-design step by learning image features directly from training data. The present work benchmarks lightweight CNN backbones and applies the best-performing model to RFC control and RFC-del live-cell PCNA datasets. Although developed and evaluated in HeLa cells, the long-term objective of this approach is to establish a computational workflow that can subsequently be adapted to other biological imaging systems, including neurogenesis-related microscopy datasets.

METHODS

Cell culture and immunofluorescence staining

HeLa cells were kindly provided by J. W. Dobrucki. Cells were cultured in DMEM medium supplemented with 10% fetal bovine serum and 1% penicillin-streptomycin at 37°C and 5% CO_2. Cells were seeded on glass coverslips and grown to 70% confluence. Cells were fixed with 4% paraformaldehyde for 15 min and permeabilized with 0.1% Triton X-100 for 10 min. Cells were blocked with 5% bovine serum albumin for 1 h and incubated with a mouse monoclonal anti-PCNA antibody (clone PC10; Abcam, catalogue no. ab29; 1:1000 dilution) overnight at 4°C. Cells were washed three times with PBS and incubated with a goat anti-mouse Alexa Fluor 488-conjugated secondary antibody (Thermo Fisher Scientific/Invitrogen, catalogue no. A-11001; 1:2000 dilution) for 1 h at room temperature. Cells were counterstained with DAPI (1:10000 dilution) for 10 min and mounted with VECTASHIELD antifade reagent. No human participants or animal subjects were used in this study.

Image acquisition and preparation

Images were acquired using a Zeiss Cell Observer Spinning Disc microscope with a 63× oil-immersion objective and a Photometrics Evolve 512 camera. ZEN software was used for microscope control and image acquisition. Z stacks were acquired at 0.24 micrometer optical spacing. Images were captured at 512 × 512 pixel resolution with 16-bit depth and saved as TIFF files. Single-cell crops were obtained by removing the background outside individual nuclei and were resized to 128 × 128 pixels. The fixed-cell dataset contained 4,934 training-folder images and 571 held-out test images; training and test images were separated at the cell level before benchmarking. To minimize information leakage, the training and test sets were generated before model training and remained unchanged throughout the study, and each single-cell crop was assigned exclusively to one dataset and was never reused across the training, validation, or test subsets. During benchmarking, a stratified 10% validation split was drawn from the training folder using seed 1337. Augmentation was applied only to training batches. Dataset class counts are shown in Table 1.

Dataset annotation

Ground-truth labels were assigned manually on the basis of characteristic PCNA staining patterns corresponding to G1, early S, mid S, and late S-phases. Annotation was performed by two investigators experienced in PCNA replication patterns, with final labels established by consensus. Cells displaying ambiguous morphology or insufficient image quality were excluded from the dataset.

Table 1. Fixed-cell PCNA dataset class counts. The validation row is the stratified 10% split drawn from the training folder during benchmarking with seed 1337.

Split	G1	early S	mid S	late S	Total
Train folder	1238	1231	1234	1231	4934
Validation split	124	123	124	123	494
Test folder	140	151	142	138	571

CNN algorithm

Four lightweight tf.keras architectures were benchmarked for 4-way classification: MobileNetV2 (Sandler et al., 2018), MobileNetV3Small, MobileNetV3Large (Howard et al., 2019), and EfficientNetB0 (Tan & Le, 2019). Models used ImageNet initialization, 128 × 128 crops, batch size 16, Adam optimization, a 10-epoch classifier-head phase with learning rate 1e-3, and a 20-epoch fine-tuning phase with learning rate 1e-4. Early stopping used patience 5. Batch-normalization layers were kept frozen during fine-tuning.

Performance evaluation

Benchmark performance was summarized by parameter count, best validation accuracy, test accuracy, macro-F1, mid S recall, and inference time per image. Precision, recall, F1-score, and support were reported for each class and each lightweight model. The MobileNetV2 confusion matrix was generated from the saved weights and the held-out fixed-cell test set.

RFC time-lapse analysis

MobileNetV2 was applied to the RFC control live-cell PCNA dataset and the RFC-del live-cell PCNA dataset. RFC-del refers to a previously generated EGFP-tagged RFC1/p140 construct lacking amino acids 367-493, corresponding to the DNA-binding region described by Hashiguchi et al. (2007); the construct was generated in-house from a pEGFP-N1-RFC1 plasmid by deletion mutagenesis and verified by Western blotting. This alteration affects the DNA-binding region of the large RFC subunit rather than deleting the entire RFC complex. The construct was used as a functional perturbation of the RFC-PCNA pathway and was not intended to model a specific neurological disorder. For each cell, class probabilities were averaged across Z slices at each time point. Class-probability traces were smoothed with a five-point moving-average filter using np.convolve with mode='same'. Cells were retained when the smoothed late S probability peak exceeded 0.2, a quality filter selecting traces with detectable late S signal. width_late_min was defined as the width of the dominant late S probability peak in minutes; width_mid_min was defined as the width of the dominant mid S probability peak in minutes; distance_late_mid_min was defined as the time difference between the dominant late S and mid S peaks. Negative distance_late_mid_min values indicate that the late-like peak occurred before the mid-like peak in the smoothed probabilistic trace. Duration summaries are medians with 95% bootstrap confidence intervals, and group comparisons use two-sided Mann-Whitney U tests; effect sizes are reported as rank-biserial correlations (|r|) and exact U statistics are given in Table 4. The RFC control and RFC-del live-cell datasets were each acquired in a single time-lapse experiment (one control and one RFC-del experiment), with multiple cells imaged across several fields per experiment; per-cell sample sizes after quality filtering are given in Table 4.

RESULTS

The lightweight benchmark showed that MobileNetV2 provided the best balance of accuracy and efficiency for PCNA-based subphase classification (Table 2). Its test accuracy was 0.901926 and macro-F1 was 0.902858, with 2.26 million parameters and 9.141 ms/image inference time in the benchmark run.

Class-wise precision, recall, and F1-score are shown for all lightweight models in Table 3. The mid S class was consistently the most difficult class; for MobileNetV2, mid S recall was 0.7324, likely reflecting the continuity of PCNA patterns and annotation boundaries between early S, mid S, and late S.

Representative PCNA staining patterns for the four fixed-cell classes are shown in Fig. 1.

The MobileNetV2 confusion matrix shows strong performance for G1 and late S and confirms that most mid S errors were assigned to early S (Fig. 2). This pattern is consistent with gradual transitions in PCNA

Table 2. Benchmark of lightweight CNN architectures for PCNA-based subphase classification.

Model	Params	Best val acc (%)	Test acc (%)	Macro-F1	mid S recall	ms/image
MobileNetV2	2,263,108	94.53	90.19	0.903	0.732	9.141
MobileNetV3Large	3,000,196	97.57	89.14	0.891	0.711	7.921
EfficientNetB0	4,054,695	97.98	88.97	0.888	0.648	11.547
MobileNetV3Small	941,428	96.15	86.51	0.861	0.592	5.258

Table 3. Per-class precision, recall, and F1-score for all lightweight models on the fixed-cell test set.

Model	Class	Precision	Recall	F1-score	Support
MobileNetV2	G1	0.9784	0.9714	0.9749	140
MobileNetV2	early S	0.7713	0.9603	0.8555	151
MobileNetV2	mid S	0.9541	0.7324	0.8287	142
MobileNetV2	late S	0.9630	0.9420	0.9524	138
MobileNetV3Large	G1	1.0000	0.9214	0.9591	140
MobileNetV3Large	early S	0.7956	0.9536	0.8675	151
MobileNetV3Large	mid S	0.9099	0.7113	0.7984	142
MobileNetV3Large	late S	0.9000	0.9783	0.9375	138
EfficientNetB0	G1	1.0000	0.9500	0.9744	140
EfficientNetB0	early S	0.7588	1.0000	0.8629	151
EfficientNetB0	mid S	0.9388	0.6479	0.7667	142
EfficientNetB0	late S	0.9362	0.9565	0.9462	138
MobileNetV3Small	G1	0.9577	0.9714	0.9645	140
MobileNetV3Small	early S	0.7411	0.9669	0.8391	151
MobileNetV3Small	mid S	0.8936	0.5915	0.7119	142
MobileNetV3Small	late S	0.9275	0.9275	0.9275	138

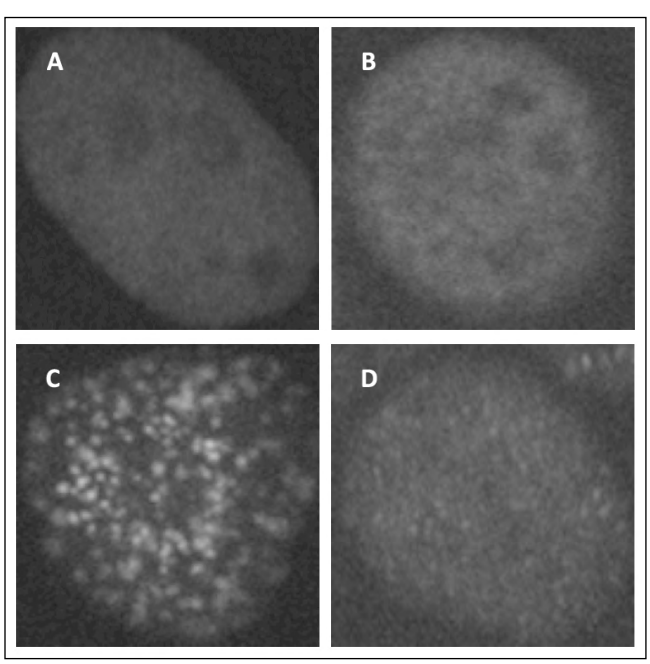

Fig. 1. Representative PCNA staining patterns used for fixed-cell class annotation: (A) G1, (B) early S, (C) mid S, and (D) late S.

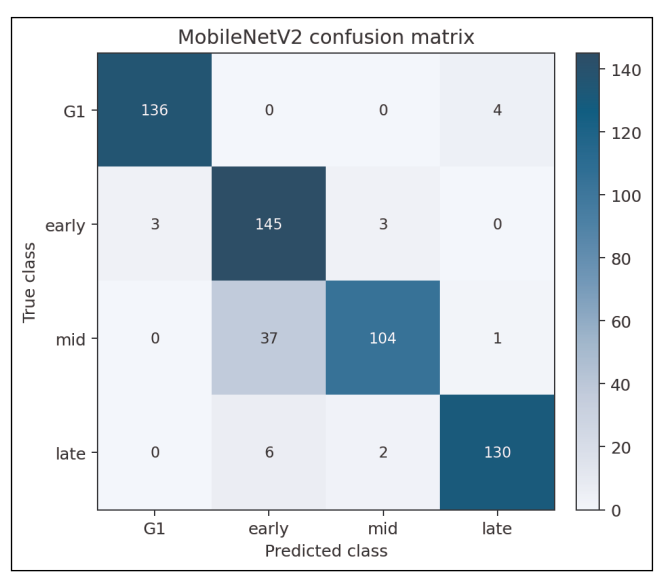

Fig. 2. MobileNetV2 confusion matrix generated from the saved weights and the held-out fixed-cell PCNA test set.

foci and annotation boundaries between early S and mid S; the confusion matrix shows 37 mid S cells classified as early S.

Fresh MobileNetV2-based time-lapse analysis included 221 RFC control cells and 60 RFC-del cells after late-peak filtering. RFC-del was associated with prolonged late S-like PCNA pattern duration. In contrast, width_mid_min and distance_late_mid_min were near-significant but did not cross P<0.05, supporting cautious interpretation and the need for a larger RFC-del sample (Table 4).

The duration plot summarizes the median and 95% confidence interval for each RFC control and RFC-del duration metric (Fig. 3). The complete analytical workflow is summarized schematically in Fig. 4.

Table 4. Median duration metrics for RFC control and RFC-del (RFC1/p140 DNA-binding-domain deletion mutant) cells with 95% bootstrap confidence intervals. Group comparisons used two-sided Mann-Whitney U tests; exact U statistics and rank-biserial effect sizes (|r|) are reported. RFC control n=221 cells, RFC-del n=60 cells.

Metric	RFC median (95% CI)	RFC-del median (95% CI)	P value	U	Rank-biserial |r|
width_late_min	344.7 (288.8 – 424.8)	517.2 (447.8 – 697.3)	0.0047	5052.0	0.238
width_mid_min	92.8 (81.7 – 103.1)	77.2 (75.7 – 80.9)	0.0568	7694.0	0.160
distance_late_mid_min	-30.0 (-60.0 – 45.0)	75.0 (-45.0 – 120.0)	0.0545	5556.5	0.162

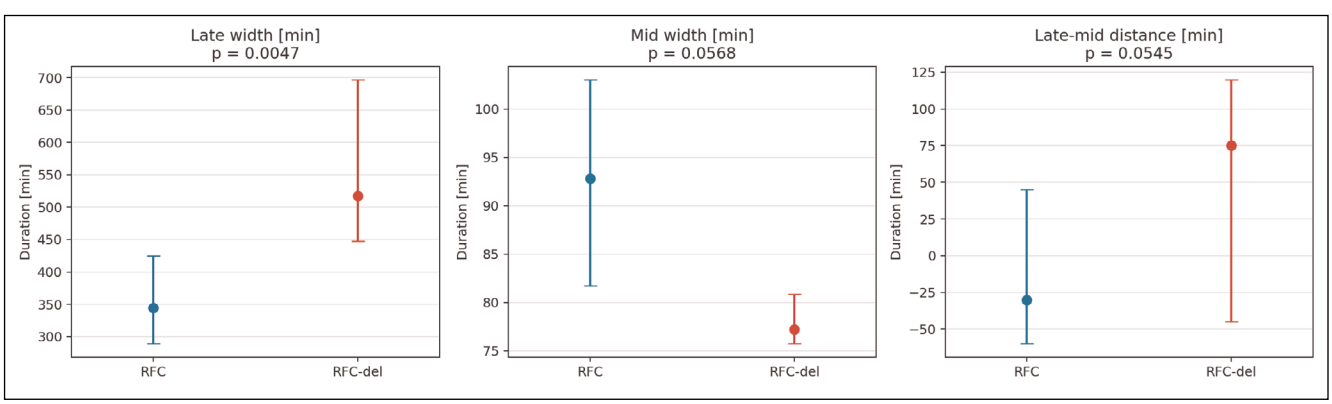

Fig. 3. Median duration of width_late_min, width_mid_min, and distance_late_mid_min in RFC control and RFC-del (RFC1/p140 DNA-binding-domain deletion mutant) cells. Points indicate medians and error bars show 95% bootstrap confidence intervals; P values are shown in the panel titles.

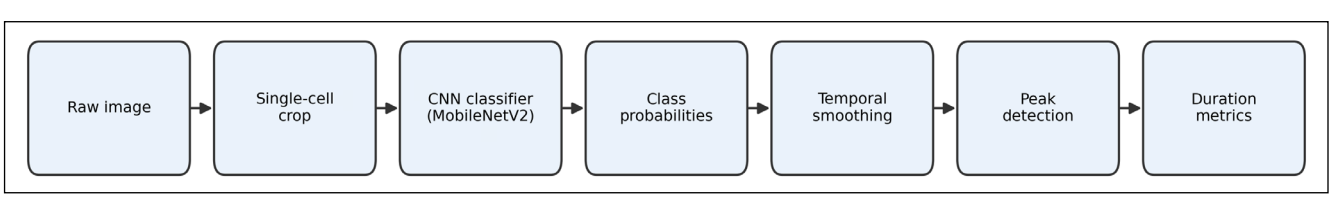

Fig. 4. Schematic overview of the analytical workflow. Each raw image is reduced to a single-cell crop, classified by the MobileNetV2 CNN into G1, early S, mid S, or late S, and the resulting class-probability traces are temporally smoothed; peak detection on the smoothed traces yields the duration metrics used for the RFC control *versus* RFC-del comparison.

DISCUSSION

This study shows that lightweight CNNs are sufficient for PCNA-based S-phase subphase classification. MobileNetV2 achieved the highest test accuracy and macro-F1 among the evaluated models while keeping inference cost low enough for iterative time-lapse scoring.

The RFC-del analysis links classifier output to the RFC-PCNA axis. RFC loads PCNA onto primed DNA in an ATP-dependent clamp-loading reaction, and PCNA then acts as a platform for DNA polymerases and other genome-maintenance factors (Yao & O'Donnell, 2012). In RFC-del cells, residues 367-493 of RFC1/p140, the large RFC subunit, are removed; Hashiguchi et al. (2007) described this region as the RFC140 DNA-binding domain. The observed prolongation of classifier-defined late S-like PCNA patterns is consistent with altered RFC-PCNA pathway function. However, the present analysis does not directly measure replication kinetics and therefore should not be interpreted as evidence for a specific molecular mechanism.

The result should nevertheless be interpreted as a change in classifier-defined PCNA image states, not as direct measurement of an RFC molecular mechanism. PCNA also participates in DNA repair, chromatin remodeling, and replication-fork biology, so PCNA-only phenotypes can integrate several processes beyond canonical DNA synthesis (Essers et al., 2005; Moldovan et al., 2007; Li et al., 2018). The mid S class remained the most difficult class for the CNN, consistent with gradual transitions in PCNA foci and uncertainty at annotation boundaries between early S, mid S, and late S.

The efficiency of MobileNetV2 suggests that lightweight PCNA-pattern classifiers could be adapted for high-content imaging. One potential future application of the proposed workflow is automated quantification of proliferating neural stem and progenitor cells. Because PCNA is commonly used as a marker of cell-cycle progression in neurogenesis studies, automated classification of PCNA patterns could facilitate large-scale image analysis in developmental and regenerative neuroscience. Such applications would require retraining and validation on neural datasets and are therefore beyond the scope of the present study.

Several limitations should be considered. First, classifier performance was established using fixed-cell images, whereas the downstream RFC analyses were performed on live-cell datasets; this fixed-cell to live-cell transfer should be validated in future experiments with matched live-cell labels. Second, the dataset split was performed at the single-cell level rather than at the level of microscopic fields, so the possibility that crops from the same field contributed to different partitions cannot be fully excluded. Third, the RFC-del group was substantially smaller than the control group after quality filtering (RFC control n=221, RFC-del n=60). Fourth, the extracted metrics represent classifier-derived image-state dynamics rather than direct measurements of DNA replication. Fifth, each RFC condition derived from a single biological experiment comprising many cells across several fields, so the analysed cells represent technical rather than fully independent biological replicates, and the RFC-dependent differences should be read as within-experiment effects pending biological replication. Consequently, biological interpretation should remain cautious until independent validation datasets become available.

CONCLUSIONS

Lightweight CNNs can classify PCNA-based S-phase subphases with high performance and can be reused for live-cell PCNA trace analysis. The RFC-del result supports an association with prolonged late S-like PCNA pattern duration and provides a reproducible starting point for larger RFC-PCNA perturbation studies.

ACKNOWLEDGMENTS

Microscopy measurements were performed at the Laboratory of Imaging Tissue Structure and Function, which serves as an imaging core facility at the Nencki Institute of Experimental Biology and is part of the infrastructure of the Polish Euro-BioImaging Node. The Polish Node is supported by the project co-financed by the Minister of Education and Science based on contract No. 2022/WK/05 (Polish Euro-BioImaging Node "Advanced Light Microscopy Node Poland"). This article is funded by the National Science Centre in Poland under project UMO-2016/21/N/NZ3/03272.

DATA AND CODE AVAILABILITY

The source code for the lightweight CNN benchmark and the live-cell PCNA trace analysis, together with the trained MobileNetV2 model weights, is available from the corresponding author upon reasonable request. The fixed-cell PCNA image dataset and the RFC control and RFC-del time-lapse datasets are likewise available from the corresponding author upon reasonable request.

REFERENCES

Essers, J., Theil, A. F., Baldeyron, C., van Cappellen, W. A., Houtsmuller, A. B., Kanaar, R., & Vermeulen, W. (2005). Nuclear dynamics of PCNA in DNA replication and repair. *Molecular and Cellular Biology, 25*(21), 9350–9359. https://doi.org/10.1128/MCB.25.21.9350-9359.2005

Haralick, R. M., Shanmugam, K., & Dinstein, I. (1973). Textural features for image classification. *IEEE Transactions on Systems, Man, and Cybernetics, SMC-3*(6), 610–621. https://doi.org/10.1109/TSMC.1973.4309314

Hashiguchi, K., Matsumoto, Y., & Yasui, A. (2007). Recruitment of DNA repair synthesis machinery to sites of DNA damage/repair in living human cells. *Nucleic Acids Research, 35*(9), 2913–2923. https://doi.org/10.1093/nar/gkm115

Howard, A., Sandler, M., Chen, B., Wang, W., Chen, L.-C., Tan, M., Chu, G., Vasudevan, V., Zhu, Y., Pang, R., Adam, H., & Le, Q. (2019). Searching for MobileNetV3. In 2019 *IEEE/CVF International Conference on Computer Vision* (ICCV) (pp. 1314–1324). IEEE. https://doi.org/10.1109/ICCV.2019.00140

Kelman, Z. (1997). PCNA: Structure, functions and interactions. *Oncogene, 14*(6), 629–640. https://doi.org/10.1038/sj.onc.1200886

Li, M., Xu, X., Chang, C.-W., Zheng, L., Shen, B., & Liu, Y. (2018). SUMO2 conjugation of PCNA facilitates chromatin remodeling to resolve transcription-replication conflicts. *Nature Communications, 9*, 2700. https://doi.org/10.1038/s41467-018-05236-y

Moldovan, G.-L., Pfander, B., & Jentsch, S. (2007). PCNA, the maestro of the replication fork. *Cell, 129*(4), 665–679. https://doi.org/10.1016/j.cell.2007.05.003

Sandler, M., Howard, A., Zhu, M., Zhmoginov, A., & Chen, L.-C. (2018). MobileNetV2: Inverted residuals and linear bottlenecks. In 2018 *IEEE/CVF Conference on Computer Vision and Pattern Recognition* (pp. 4510–4520). IEEE. https://doi.org/10.1109/CVPR.2018.00474

Schönenberger, F., Deutzmann, A., Ferrando-May, E., & Merhof, D. (2015). Discrimination of cell cycle phases in PCNA-immunolabeled cells. *BMC Bioinformatics, 16*, 180. https://doi.org/10.1186/s12859-015-0618-9

Tan, M., & Le, Q. V. (2019). EfficientNet: Rethinking model scaling for convolutional neural networks. *Proceedings of the 36th International Conference on Machine Learning, 97*, 6105–6114.

Yao, N. Y., & O'Donnell, M. (2012). The RFC clamp loader: Structure and function. In S. MacNeill (Ed.), The eukaryotic replisome: A guide to protein structure and function (*Subcellular Biochemistry, Vol. 62*, pp. 259–279). Springer. https://doi.org/10.1007/978-94-007-4572-8_14

Zerjatke, T., Gak, I. A., Kirova, D., Fuhrmann, M., Daniel, K., Gonciarz, M., Müller, D., Glauche, I., & Mansfeld, J. (2017). Quantitative cell cycle analysis based on an endogenous all-in-one reporter for cell tracking and classification. *Cell Reports, 19*(9), 1953–1966. https://doi.org/10.1016/j.celrep.2017.05.022

Zhang, J., & Jiao, J. (2015). Molecular biomarkers for embryonic and adult neural stem cell and neurogenesis. *BioMed Research International, 2015*, 727542. https://doi.org/10.1155/2015/727542